Supporting information

Coherent Structured Illumination Provides a Lateral Resolution of sub-100 nm in Light Sheet-based Fluorescence Microscopy: csiLSFM

Bo-Jui Chang, Victor Didier Perez Meza, and Ernst H.K. Stelzer*

Physical Biology (FB 15, IZN), Buchmann Institute for Molecular Life Sciences (BMLS, CEF-MC), Goethe Universität Frankfurt am Main (Campus Riedberg), Max-von-Laue-Strasse 15, D-60438 Frankfurt am Main, Germany

*Correspondence should be addressed to: ernst.stelzer@physikalischebiologie.de

This file includes:

Materials and Methods

Figs. S1 to S23

Tables S1 to S2

Note 1: Materials and Methods

Experimental setup

A conventional light sheet microscope (aka single/selective plane illumination microscope, SPIM) uses a cylindrical lens and an objective lens(1) to generate the light sheet. Essentially, we implement two SPIM-based identical illumination arms (Fig. 2, A and B) to generate two counter-propagating light sheets. The main optical components of each illumination arm in our setup include a cylindrical lens, a coupling lens, a scanning mirror, an f-θ lens and an objective lens. The fiber collimator delivers the linearly polarized and collimated laser beam required for coherent structured illumination. The choice of the optical components determines the thickness and the length of the light sheet, as well as the achievable rotation angle of the interference pattern. The thickness of our light sheet is ~2.6 µm, which corresponds to a Rayleigh region 11.2 µm long and a divergence of 6.75°, with the current combination of cylindrical lens, coupling lens, and collimator. The same objective lens is used in the detection path to acquire the fluorescence image. In combination with the 1x tube lens (45 29 60, Carl Zeiss) and the sCMOS camera (C11440, ORCA-Flash 2.8, Hamamatsu), one pixel on the camera corresponds to 57.6 nm in the focal plane of the 63× objective lens (3.63 µm/63). It is important to have a small pixel size to present the image with a reasonable contrast and resolution without compromising the fluorescence intensity. Our pixel size meets the reasonable pixel size of about 60 nm in a wide-field fluorescence microscopy as described previously in the literature(2) but notoriously ignored in many experiments. We use an emission filter to block the laser for the observation of the fluorescence signal (FF02-525/50-25, Semrock). Additionally, an optical filter glass (OG530, SCHOTT), which happens to pass a small portion of laser intensity, is used to examine the interference pattern. The optomechanical parts of the main system are mounted on two rail systems (SYS40, SYS65, OWIS). A photograph of our system is shown in fig. S5.

Embedding samples in gel

Both agarose gel and phytagel can be used as embedding substrates in our system. For the preparation of agarose gel, we use low melt agarose (6351.5, Carl Roth) because of its lower congealing temperature of around 30°C. Phytagel congeals at a temperature below 65°C when dissolved in PBS buffer. This temperature is too high for both latex beads and biological specimens. Therefore, we developed another method by adding phytagel powder into DI water containing 2.5 mM calcium ions. This method keeps the phytagel in a liquid phase at the lowest temperature of about 45°C. We usually prepare the Phytagel at a concentration of 0.5% or 1%.

SIM Reconstruction algorithm

The reconstruction algorithm is essentially the same as that used in a conventional SIM. Yet, we modified a few steps and verified that it improves the image quality(3). First, we deconvolve each raw image with the Richardson-Lucy (RL) algorithm. Next, the main reconstruction is performed as described in the literature(4–6). The deconvolved raw images are Fourier transformed. The spectrum of each raw image contains high-frequency information ($\tilde{S}_j^{\pm}(\vec{k} \pm \vec{p}_j)$) but it is mixed with wide-field information $\tilde{S}^{o}(\vec{k})$ originally in the OTF (Fig. S1, B3). To separate the high frequency information, three raw images in each orientation are required and processed in a 3x3 system of linear equations(4, 5). The precise pattern frequency $\overrightarrow{p_j}$ and the common starting phase φ_{j0} (j indexes orientation) in each set of patterns are required in the 3x3 linear system. The pattern frequency $\overrightarrow{p_j}$ is obtained by seeking a peak in the cross-correlations of $\tilde{S}^{o}(\vec{k})$ and $\tilde{S}_j^{\pm}(\vec{k} \pm \vec{p}_j)$ (Fig. S21). This is possible since the common starting phase φ_{j0} acts only as a scaling factor for $\tilde{\boldsymbol{S}}^{o}(\vec{k}) * \tilde{\boldsymbol{S}}_j^{\pm}(\vec{k} \pm \vec{p}_j)$. The position of the peak is independent of the starting phase of the illumination pattern. After retrieving the pattern frequency $\overrightarrow{p_j}$, the value of φ_{j0} can be recovered with several methods(4, 6). Here, we simply compare the SI-image reconstructed at

different values of φ_{j0} from 0 to 2π with the wide-field image in real space. The correct value of φ_{j0} is found when the SI-image and the wide-field image are similar, *i.e.* the normalized cross-correlation of SI-image and wide-field image has a maximum. The PSF used in the initial deconvolution is created with the *Diffraction PSF* plugin of ImageJ(7). The initial deconvolution removes the out-of-focus fluorescence to a certain extent. It reveals frequencies that are weak and hidden in the original background intensity thus supporting the search for the peak in the cross-correlations of $\tilde{S}^{o}(\vec{k})$ and $\tilde{S}_{j}^{\pm}(\vec{k} \pm \vec{p}_{j})$ especially when the pattern is extremely fine. An improvement of the resolution is not the issue in this initial deconvolution. After the reconstruction, the deconvolution is continued with a calculated PSF based on the corresponding SIM image, i.e. the pattern period and orientations correspond to the exact experimental condition. The continued deconvolution also relies on the RL algorithm. We use less than ten iterations of the RL algorithm in both deconvolutions to avoid any artefacts. In our experience, ~20 iterations suffice for a good reconstruction whereas using higher numbers produces deconvolution related artifacts (Fig. S23).

RL deconvolution is applied in many astronomy- and microscopy-related image processing algorithms and regarded as reliable and effective(8–14). A maximum-likelihood image restoration has also been successfully applied in LSFM image(15). A modified RL deconvolution (jRL, joint RL algorithm) has also been demonstrated successfully in multifocal SIM(12, 16). The continued deconvolution functions similarly to the Wiener deconvolution commonly used in SIM reconstruction, which decreases the noisy patches but without any subjective selection of the Wiener parameter. It has been reported that the Wiener parameter improves or affects the final resolution of SI images(17). RL deconvolution simplifies the whole image reconstruction process. Finally, LSFM images are well suited for deconvolution due to their excellent signal-to-noise ratio, i.e. their high dynamic range(10).

Image presentation

The summedWF represents a conventional wide-field image reconstructed by summing all raw images. The decWF image represents the deconvolution of the conventional wide-field image. It is obtained as part of the reconstruction of the SI images. The deconvolution is inherent because we perform the deconvolution of each raw image in the SI reconstruction. Once an image stack was recorded, e.g. the yeast images or the image stacks of the beads, we corrected the drift of the planes by the StackReg plugin in ImageJ with the “translation transformation only” option. The final SIM images (SIall) were scaled 2x inherently during the reconstruction. The summedWF and the decWF were scaled 2x laterally in ImageJ with a bicubic interpolation. The pixel pitch is 28.8 x 28.8 nm^2. The z-stacks are also scaled to obtain the same pixel pitch along all directions, i.e. a voxel pitch of 28.8 x 28.8 x 28.8 nm^3. All summedWF and decWF images were recorded with light sheet illumination, i.e. not in an epi-fluorescence microscope.

Resolution measurement

We measured the resolution in two dimensions since we currently only improve the lateral resolution. I.e., we cropped the bead image and fitted the image with a two-dimensional Gaussian curve. We calculate the resolution as the full width at half maximum (FWHM) of the resultant Gaussian curve. All fits were performed with *Mathematica*(18). One example is shown in fig. S11. For a three-dimensional image stack, we cropped the image of each bead in its focus since this provides a precise measurement. One example is shown in fig. S13. We noticed that the average resolutions in x and y are not even similar in the summedWF image. We believe this to be caused by the drop of the gel due to the gravity during the imaging process. To correct this effect, we used the values in the summedWF and calculated the ratio of the resolutions along y and x (ratio_y/x). We used this value as a reference and calculated the final resolutions of decWF and SIM images. Figure S11 and fig. S13 illustrate the calculation in more detail.

Note 2: Concept of Structured Illumination Microscopy (SIM)

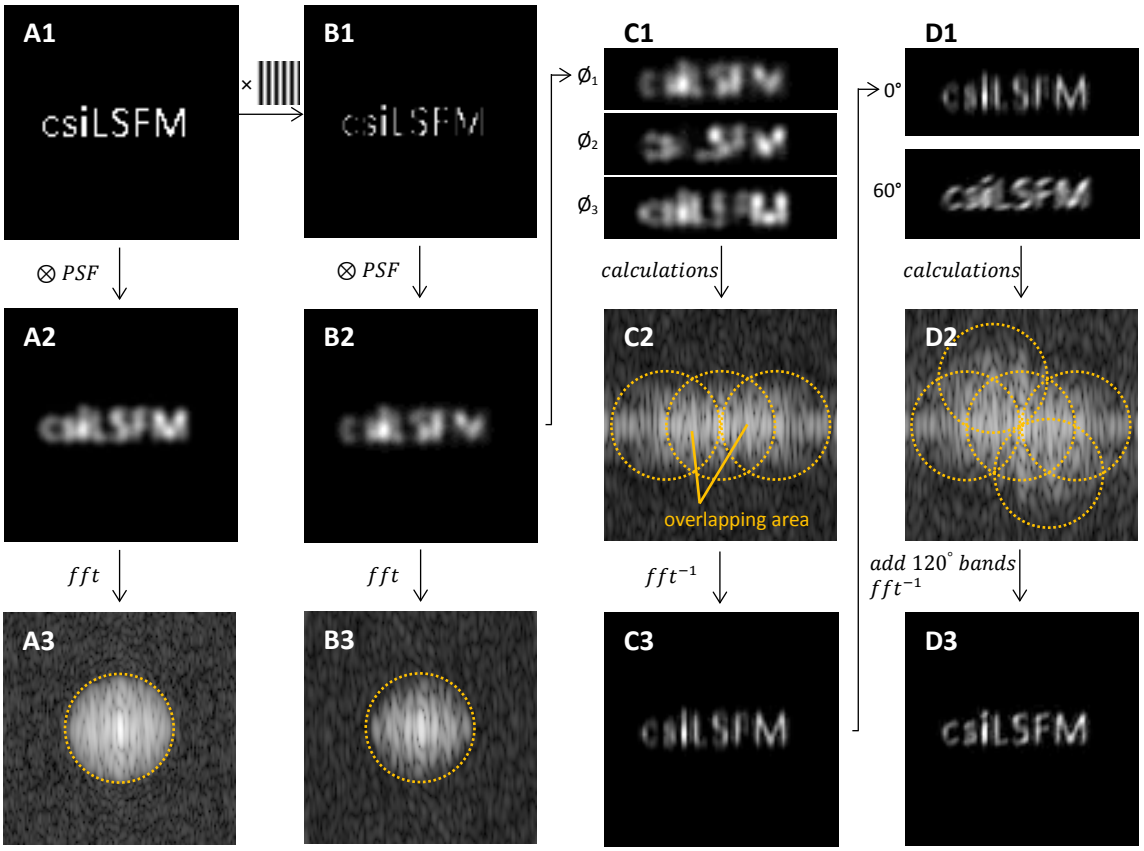

Fig. S1. Filling the k-space with structured illumination. The theory behind SIM has been described many times(5, 19, 20). The basic idea of SIM is to extend the k- or frequency-space. However, probing the k-space by illuminating the fluorescent specimen with a fixed pattern is not sufficient. The pattern's phase has to be varied precisely and systematically, thus, several images need to be recorded in order to resolve the ambiguities when assigning the energies to their corresponding locations in k-space. This process has to be performed in the entire two- or three-dimensional k-space and requires the observation of a fluorescent specimen along multiple directions. (**A1, A2**) A conventional fluorescence image (A2) is formed by convolving the point spread function (PSF) with the object (A1). (**B1, B2**) A structured illumination raw image is formed by multiplying the object with the structured pattern (B1) and then convolving it with the PSF. (**A3, B3**) The power spectra of the images (A2, B2), which denote the spatial frequency information of a conventional image. The orange circle indicates the region of the frequency band (aka optical transfer function, OTF) that can be observed. The power spectrum of a structured illumination raw image (B3) contains high-frequency information within the OTF. (**C1, C2**) To extract and extend the frequency information, at least three structured illumination raw images with three phases ($ø_1$-$ø_3$) are required. Matrix calculations resolve and separate the frequency bands, thus assigning the energies to their correct positions in k-space. E.g. the frequency information is extended in k-space along one orientation (C2). (**C3**) The inverse Fourier transform of the extended frequency information (C2) results in a high-resolution image along one direction. (**D1**) The same procedure is performed along other orientations (60°). (**D2**) By using the illumination from more orientations (0° and 60° in this example), the frequency information can be extended to the corresponding orientation. (**D3**) After the extended frequency information is completed in 360° (0°, 60° and 120° in this example), an isotropic high-resolution image can be obtained.

Note 3: Optimal resolution in a linear SIM

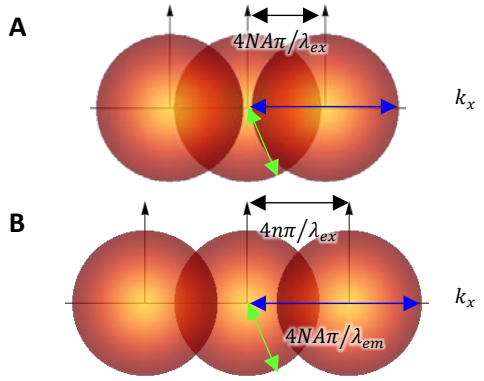

Figure S2 Optimal resolution $\lambda/4n$ is achieved with counter-propagating beams. The resolution improvement of SIM is explained in Fourier space. Only one pattern orientation is presented to illustrate the concept. The gradient disk represents the OTF of the detection lens, which is calculated by $OTF(\nu) = \frac{2}{\pi}(\cos^{-1}|\nu| - |\nu|\sqrt{1-\nu^2})$. The black, green, and blue double headed arrows represent the pattern frequency, the maximum OTF frequency, and the frequency of final resolution, respectively. The resolution improvement relies on the illumination pattern frequency. The high frequency pattern is achieved by interfering two beams. **(A)** In a conventional SIM the pattern frequency is limited by the detection objective lens. The maximum pattern frequency is $4NA\pi/\lambda_{ex}$. By substituting λ_{em} with $\alpha\lambda_{ex}$, the final resolution improvement is $\frac{4NA\pi/\lambda_{ex}+4NA\pi/\alpha\lambda_{ex}}{4NA\pi/\alpha\lambda_{ex}} \cong 2$. (**B**) The theoretical maximum pattern frequency is achieved when two beams are counter-propagating. In this case, which is achievable in csiLSFM, the pattern frequency is $4n\pi/\lambda_{ex}$. The optimal resolution improvement with the interference pattern of counter-propagating beam is $\frac{4n\pi/\lambda_{ex}+4NA\pi/\alpha\lambda_{ex}}{4NA\pi/\alpha\lambda_{ex}} \cong 2.4$. We assume α is 1.02 in the calculation ($\alpha = em/ex = 515/505$).

Note 4: Corresponding chamber for the real three objective lenses arrangement

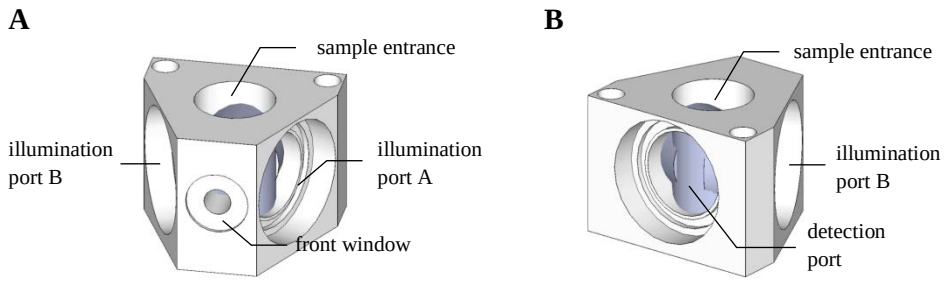

Fig. S3. Corresponding specimen chamber. (A, B) The front view and the rear view of the chamber. The specimen is inserted into the chamber and held from above. The two illumination ports allow a rotation angle of the two illumination objective lenses between 20° and 30°. The front window is used to observe the inside of the specimen chamber and to illuminate the specimen, e.g. with incoherent light required for a reasonable transmission image.

Note 5: Phase control of the interference pattern with the scanning mirrors

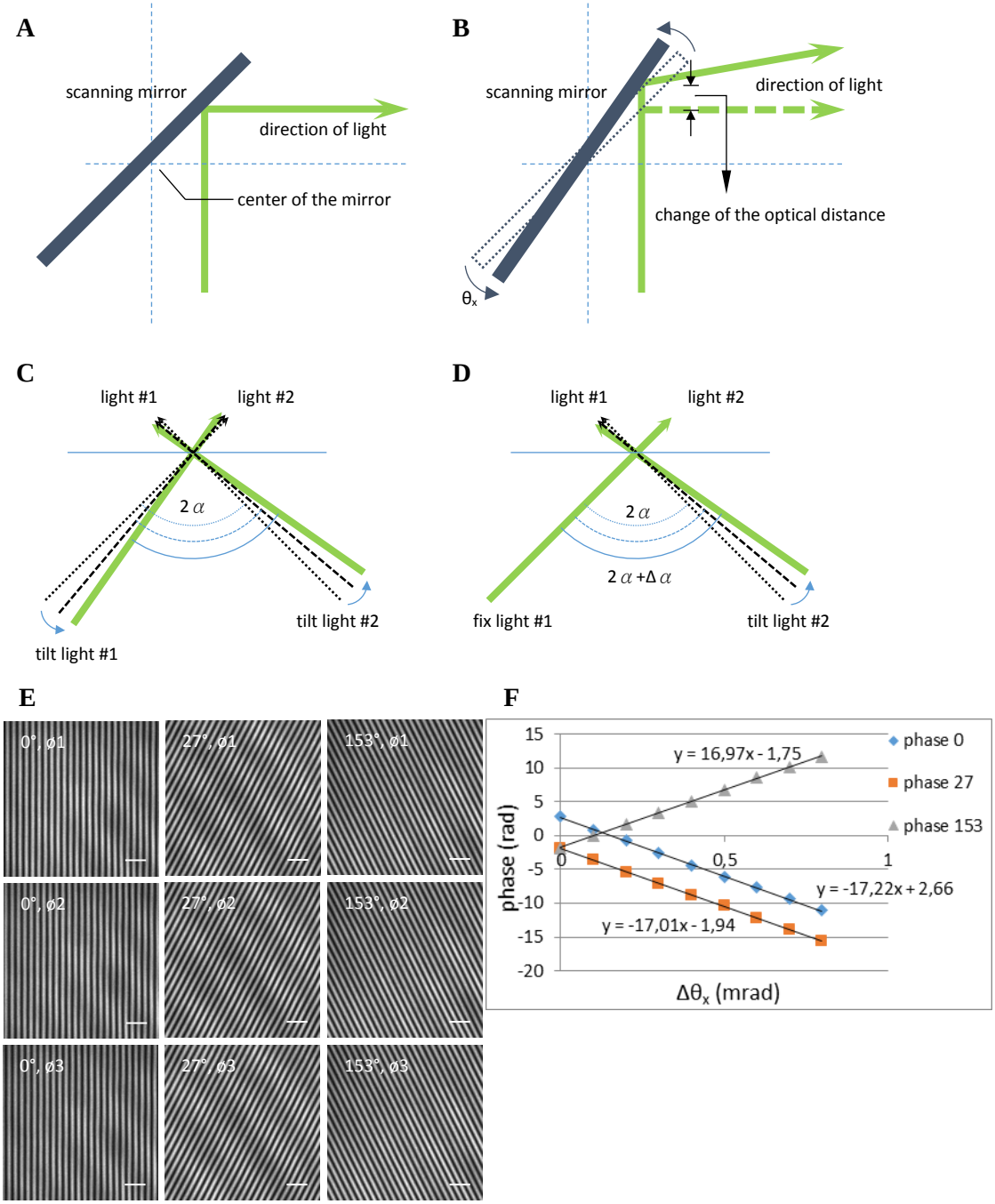

Fig. S4. Phase control of the interference pattern with the scanning mirrors. Instead of using a piezo-driven device to translate the collimator, it is also possible to control the phase of the interference pattern by the scanning mirror. The idea is to create an optical distance difference. (**A**) Ideally, the laser beam is deflected in the center of the scanning mirror but in practice, the beam is slightly off-center. (**B**) A fractional change in the angle causes a change of the optical distance and hence induces a phase shift of the interference pattern. (**C**) The simultaneous rotation of both beams merely causes a phase shift of the interference pattern. (**D**) The period of the interference pattern changes if only one beam is rotated. (**E**) The phase and the orientation of the interference pattern are, therefore, precisely controlled. The

change of the phase is $\frac{2}{3}\pi$, which provides the minimal number of three images required for a reconstruction. (**F**) One example shows the relation between the phase of the interference pattern and the small tilting angle $\Delta\theta_x$ of the scanning mirrors. The slope of the trend line measures the corresponding tilting angle to achieve the phase shift of $\frac{2}{3}\pi$ of the pattern. We tried this method but found it to demand a higher alignment precision. It is easier and more stable to control the phase shift of the interference pattern with a piezo-driven stage that moves one of the two collimators. All scale bars are 1 μm wide.

Note 6: csiLSFM bench top evaluation system

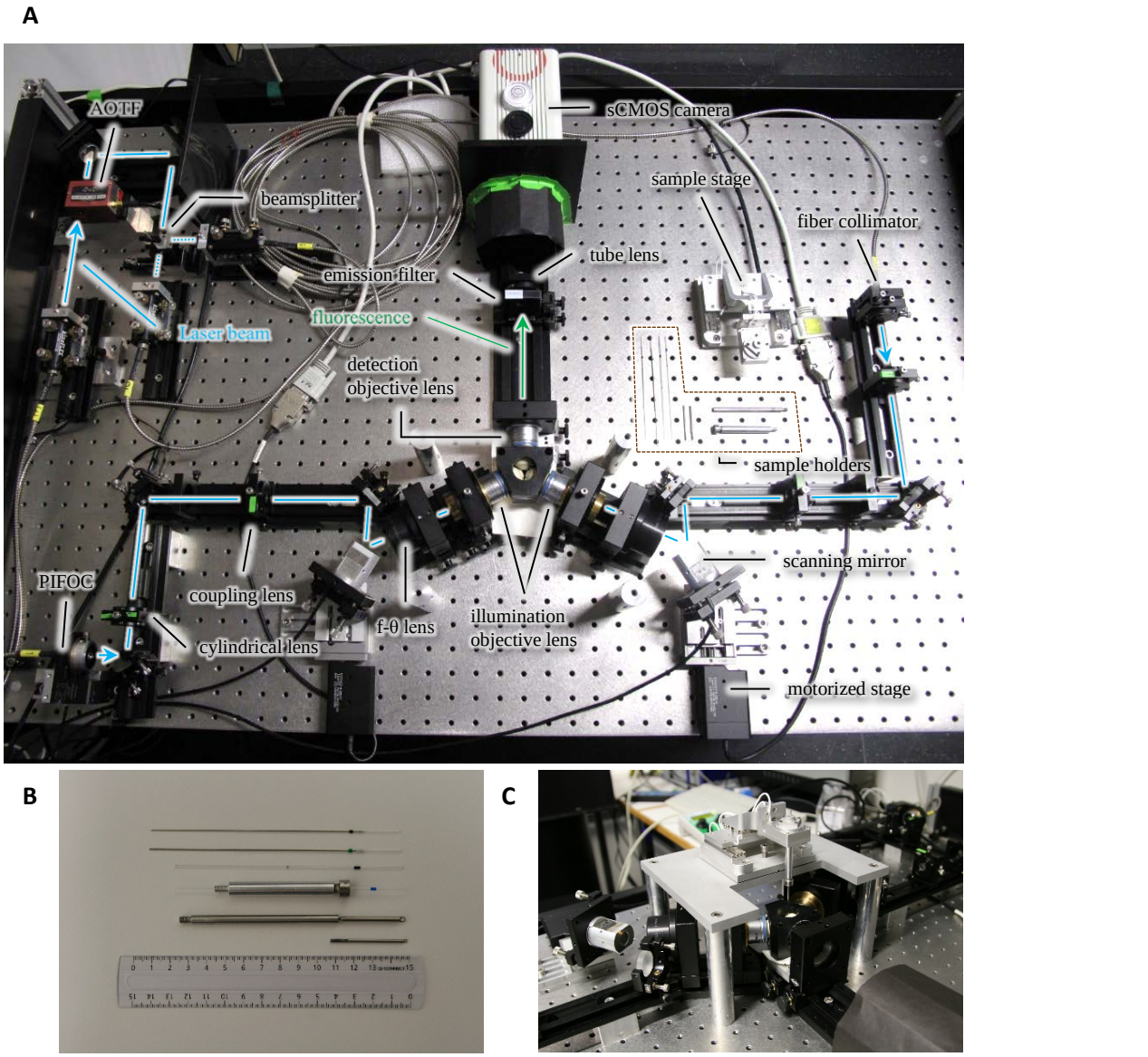

Fig. S5. Photograph of the system and the sample holder. A polarization-preserving, single-mode fiber (kineFLEX, Qioptiq) guides the laser light (35 LTL 835, Melles Griot) onto the bench top. (**A**) An acousto-optic tunable filter (AOTF, AA.AOTF.4C+AAMOD.4C, Pegasus Optik) selects the wavelength (488 nm), adjusts the laser power and switches the laser light on and off. A beam splitter provides two coherent beams, which are deflected into two polarization-preserving single-mode fibers. The laser beams exiting the two fiber outputs (F220FC-543, Thorlabs) are collimated and form the two illumination paths. The fiber collimator is carefully turned to maintain s-polarization of the light sheets when they interfere, i.e. the polarization lies in the focal plane of detection objective lens. Each illumination path consists of a cylindrical lens (f=75 mm, F69-699, Edmund Optics), several static mirrors, an achromatic lens (f=200 mm, G322327322, Qioptiq), a two-axis piezo scanning mirror (S-334.2SL, Physik Instrumente), an f-theta lens (f=60.5 mm, S4LFT0061, Sill optics) and the microscope objective lens (63×/NA1.0, W Plan-Apochromat, 421480-9900-000, Carl Zeiss). The scanning mirror is placed on a motorized stage (M-232.17, Physik Instrumente) for a more precise alignment and a more flexible control of two light sheets. In one illumination arm, the fiber collimator (left) is mounted on a piezo-driven device (P-725.4CD, Physik

Instrumente) to introduce the optical path difference that changes the phase of the interference pattern. The detection path consists of the microscope objective lens, an emission filter, a tube lens and a camera as described in the methods section. (**B**) Various sample holders are possible. From top to the bottom: black and green capillaries with plungers from Zeiss Lightsheet Z.1 microscope, black capillary (708718, BRAND), blue capillary (708744, BRAND) inside our custom-made capillary holder, custom-made ring holder with an inner diameter of 2 mm and custom-made ring holder with an inner diameter of 1 mm. (**C**) The sample holder is attached to the sample stage (custom-designed, SmarAct) and assembled on the system for imaging.

Note 7: Flexible control of intersection and rotation angles of two beams

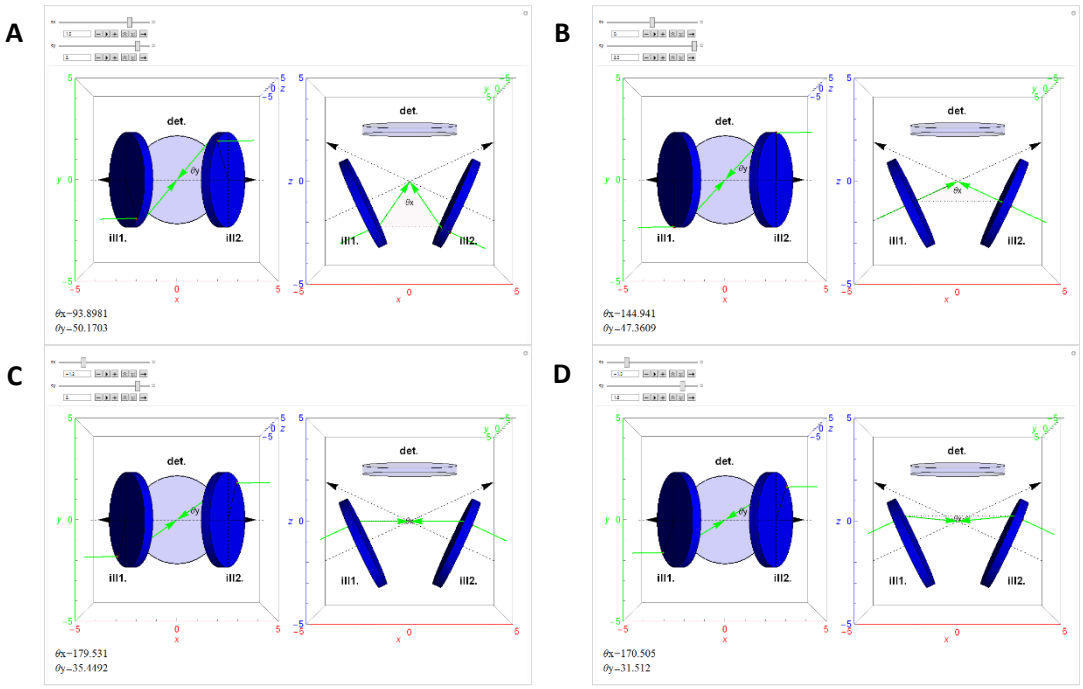

Fig. S6. Simulation of the flexible control of two beams with *Mathematica*. The figures shown here provide us with a better understanding of the intersection and rotation angles of the two beams. They indicate what can be achieved with our currently available objective lenses. The blue disks represent the objective lenses that are simulated according to the actual size of the objective lens. The arrangement of the blue disks is based on the current practical arrangement of the three objective lenses. The period of the pattern is inversely correlated with the intersection angle (θx) of two beams. A smaller intersection angle can achieve a larger rotation angle but the resolution improvement is lower. (**A**) The intersection angle is only 93.9° but the rotation angle can be up to 50°. (**B**) Beams passing through the center of the illumination objectives result in an intersection angle of about 144.9° while the rotation angle is 47.3°. The 47.3° approximately fit the acceptable angle (48.75°) of our chosen objective lens. (**C**) The intersection angle is 180° (counter-propagating beams, maximum resolution improvement) but with the current technology the rotation angle is restricted to 35°. (**D**) This illumination configuration is suitable for the specimen embedded on a coverslip. The intersection angle is 170°, close to counter-propagating condition but the rotation angle is even smaller.

Note 8: Interference patterns of two light sheets

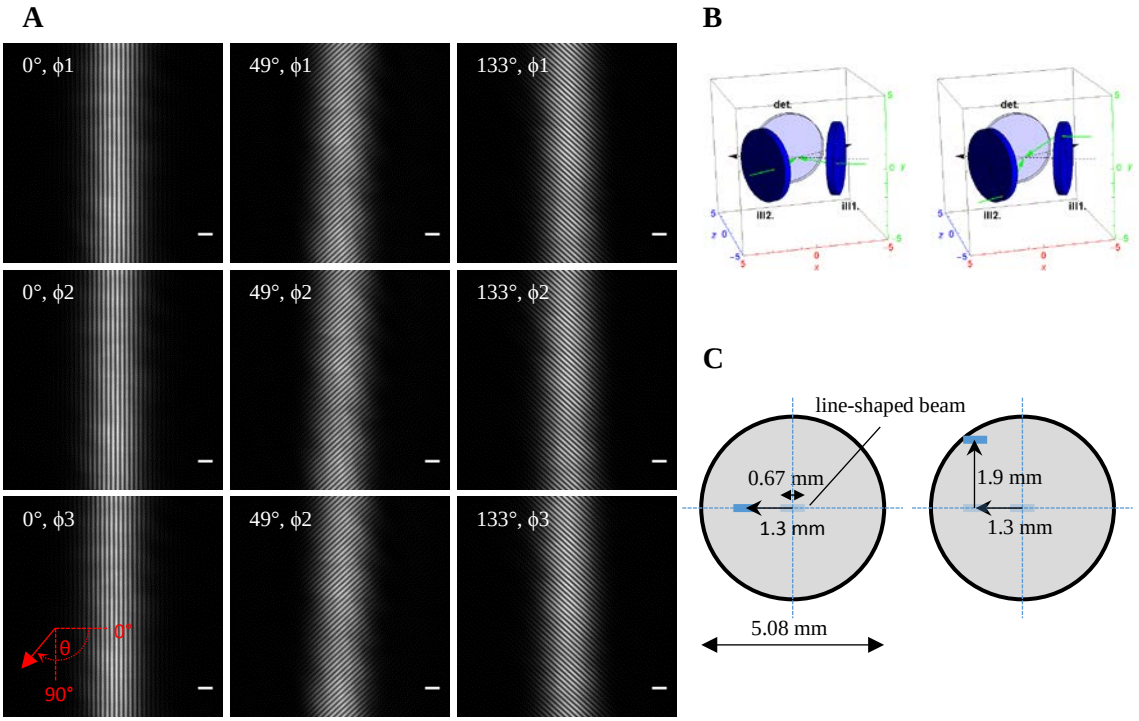

Fig. S7. Visualization of the Interference patterns. (A) Flexible control of the interference pattern generated by two light sheets in three orientations with three phase shifts. The phase shift of the interference pattern is 2/3 π in all three orientations. (**B**) To characterize the properties of the interference pattern, two collimated beams or two light sheets are manipulated to enter both illumination and detection objective lenses to visualize the pattern. These two drawings illustrate the conditions of the beams that create the patterns shown in (A). The drawings present the configurations for creating the pattern of 0° orientation and the maximal orientations, e.g. 49°, respectively. (**C**) The two sketches illustrate the geometry of the line-shaped beam (blue line) in the back aperture (gray circle) of the objective lens. The light blue lines represent the intermediate positions of the line-shaped beam. The line-shaped beam has a width of 0.67 mm with the current choice of optical elements. In the pattern of 0° orientation, the line-shaped beam is moved horizontally by 1.3 mm with our scanning mirror to direct the light sheet into the detection objective lens. The beam is further moved vertically by about 1.9 mm, to rotate the interference pattern to about 49°. The spatial period of the interference pattern is about 301 nm in this example. All scale bars are 1 µm wide.

Note 9: Raw images of beads recorded in csiLSFM

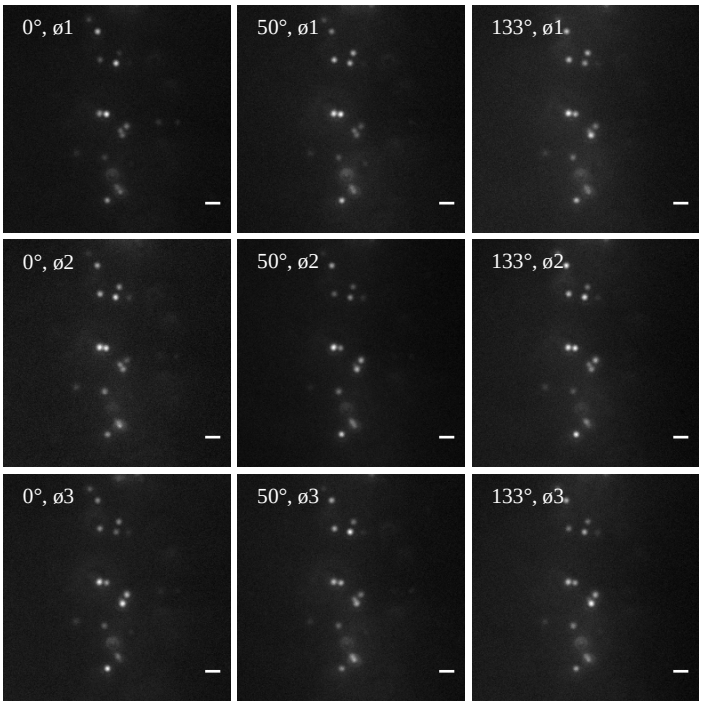

Fig. S8. Two-dimensional images recorded in csiLSFM. One example of the raw images of fluorescent latex beads with an average diameter of 40 nm embedded in 1.5% low-melt agarose illuminated with structured light sheets in three phases and three orientations. The beads have different intensities ("blinking") since the visually unresolvable pattern is moved and rotated. The intersection angle of two light sheets used for 0° pattern is 75.1° here. However, in such a small intersection angle the rotation angle of the interference pattern can be as large as simulated in fig. S6A. All scale bars are 1 µm wide.

Note 10: Isotropic high-resolution image reconstructed with 0°, 50°, and 133° patterns

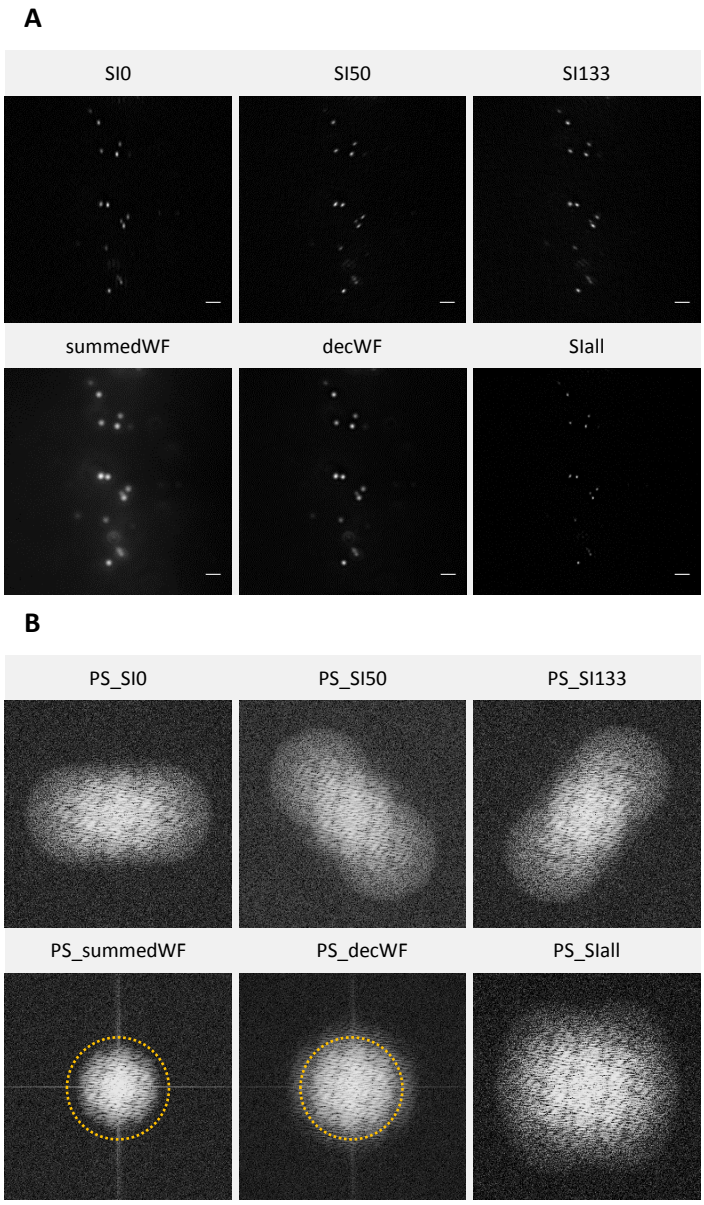

Fig. S9. Resolution improvement in csiLSFM. High-resolution images reconstructed from the raw images shown in fig. S8. (**A**) SI0, SI50, SI133 and SIall represent the SI images reconstructed with 0°, 50°, 133° and all three patterns, respectively. The summedWF and decWF represent a conventional wide-field and the deconvolution of the conventional wide-field image, respectively. The images are obtained as described in the image presentation section in Methods. All scale bars are 1 µm wide. (**B**) The power spectra (PS) of the images shown in (A). The spectra are obtained with the FFT function of ImageJ. We observe that the frequency information is extended along the corresponding pattern orientations (e.g. PS_SI0, PS_SI50, and PS_SI133). The reconstructed image with three orientations has a relatively isotropic extended frequency information (PS_SIall). Its range is approximately twice as large as that of the decWF image (PS_decWF). The orange dashed circles indicate the theoretical region of OTF calculated with emission wavelength at 515 nm, refractive index at 1.33, and NA of 1.0. Practically, the measured OTF is smaller than the theoretical one, whereas the OTF of a deconvolved image is just slightly larger than the theoretical one.

Note 11: Motorized stage helps to achieve a larger rotation angle of the pattern

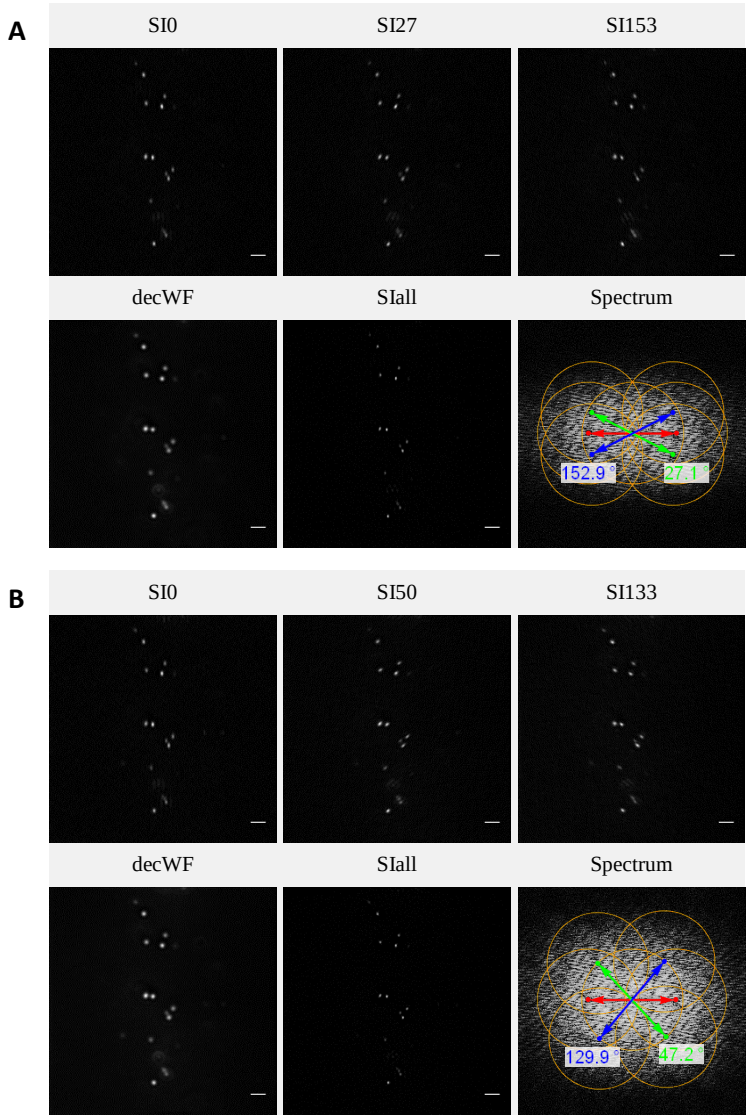

Fig. S10. Comparison of SI images with the illumination pattern between small and large rotation angle. (**A**) SI images reconstructed with 0°, 27° and 153° pattern orientations. (**B**) SI images reconstructed with 0°, 50° and 133° pattern orientation. The decWF denotes the deconvolved wide-field. The orange circles represent the region of OTF, which is calculated using 2NA⁄λ with NA=1.0 and λ=515 nm. The overlay with the spectra indicates the extended frequency information in the SIall images. The red, green and blue arrows indicate the extended frequency information of three pattern orientations, respectively. The angles represent the corresponding pattern orientations. A larger rotation orientation is realized with the help of the motorized stage shown in fig. S5A. It provides an additional manipulation of the light sheet when it is tilted to rotate the interference pattern. The SI images reconstructed from single pattern orientations (i.e. SI27, SI153, SI50, and SI133) are shown separately to compare the improvement of the reconstruction with a larger rotation angle. From the SIall images and their spectra we can already observe that the reconstruction with 0°, 50° and 133° pattern orientation is more isotropic. Nevertheless, the quantitative comparison is shown in fig. S10. The periods of three interference pattern orientations in (A) are 300.9 nm, 291.8 nm, and 291.8 nm. The periods of the interference patterns in (B) are 300.9 nm, 263.8 nm, and 262.9 nm. All scale bars are 1 µm wide.

Note 12: Quantification of the super-resolution improvement in figure S10

A

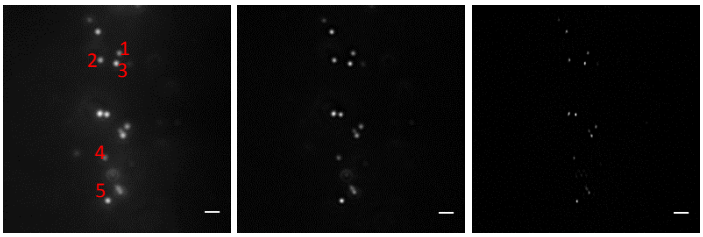

Bead1

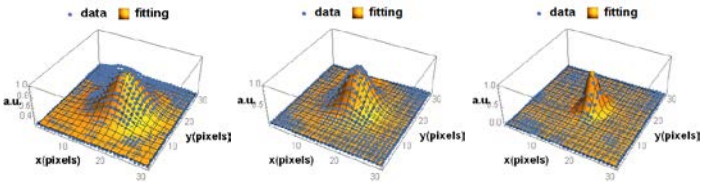

summedWF decWF SIall

	summedWF		decWF		SIall	
	x	y	x	y	x	y
Bead1	285.0	293.9	255.6	226.9	104.4	145.1
Bead2	291.7	296.0	224.5	227.5	103.8	152.1
Bead3	284.8	292.7	218.4	223.9	82.7	154.0
Bead4	313.0	320.9	248.0	252.4	89.6	149.6
Bead5	288.3	280.8	215.3	209.2	91.1	125.3
Avg	**292.6**	**296.9**	**226.4**	**228.0**	**94.3**	**145.2**
STDEV	**11.77**	**14.69**	**12.83**	**15.55**	**9.48**	**11.62**
ratio_y/x		**1.01**		1.01		1.54
correction	**292.6**	**292.6**	**226.4**	**224.7**	**94.3**	**143.1**

B

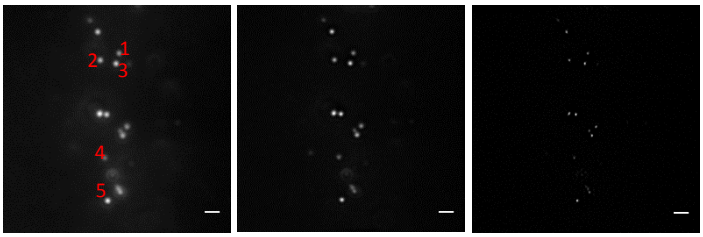

Bead1

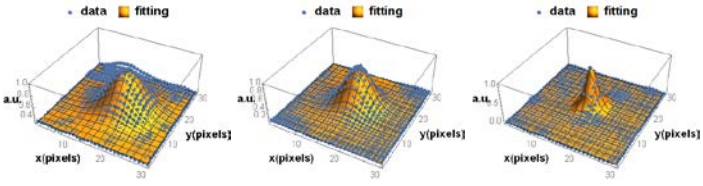

summedWF decWF SIall

	summedWF		decWF		SIall	
	x	y	x	y	x	y
Bead1	288.7	290.9	231.3	227.7	104.8	130.4
Bead2	297.3	296.0	231.0	228.1	112.0	114.6
Bead3	286.1	292.6	219.2	223.3	88.4	137.5
Bead4	312.4	322.9	246.2	256.2	109.9	151.4
Bead5	293.9	283.6	220.3	212.0	105.7	114.1
Avg	**295.7**	**297.2**	**229.6**	**229.5**	**104.2**	**129.6**
STDEV	**10.32**	**15.06**	**10.90**	**16.30**	**9.29**	**15.84**
ratio_y/x		**1.01**		1.00		1.24
correction	**295.7**	**295.7**	**229.6**	**228.3**	**104.2**	**128.9**

Fig. S11. One example of resolution measurement. We first cropped some bead images and then fitted the cropped images individually with a two-dimensional Gaussian curve. All fits are done with *Mathematica*, as shown in the second row in each panel. We only show the fit of Bead1 as an example.

The average resolutions in x and y are not similar even in the summedWF image because of the falling of the gel due to the gravity during the imaging process. Therefore, we calculated the ratio of the resolutions in y and x of summedWF (ratio_y/x row in the table). Next, we used this value as a reference and calculated the final resolutions of each image, which are shown in the last row in each table. (**A**) and (**B**) are the measurements of the images in fig. S10A and fig. S10B, respectively. Finally, we obtained the resolutions of the conventional wide-field image in (A) as 292.6±11.77 nm (x) and 292.6±14.69 nm (y). The resolutions of the deconvolved wide-field image in (A) are 226.4±12.83 nm (x) and 224.7±15.55 nm (y). The resolutions of the SIall image in (A) are 94.3±9.48 nm (x) and 143.1±11.62 nm (y). The resolutions of the conventional wide-field image in (B) are 295.7±10.32 nm (x) and 295.7±15.06 nm (y). The resolutions of the deconvolved wide-field image in (B) are 229.6±10.90 nm (x) and 228.3±16.30 nm (y). The resolutions of the SIall image in (B) are 104.2±9.29 nm (x) and 128.9±15.84 nm (y). The resolutions of summedWF and decWF images in (A) and (B) are similar. The x-resolution of SIall in (A) is slightly better than in (B). We conclude this is because there is more contribution of the frequency information of the 27° and 153° patterns in the 0° frequency information. However, the frequency information of 50° and 133° patterns contribute more into the 90° frequency information so the y-resolution of SIall in (B) is better than that in (A); meaning the high-resolution image is more isotropic. Quantitatively, the ratio of the final resolution between y and x in SIall is improved from 1.54 to 1.24.

Note 13: High-resolution image stack with laterally isotropic resolution

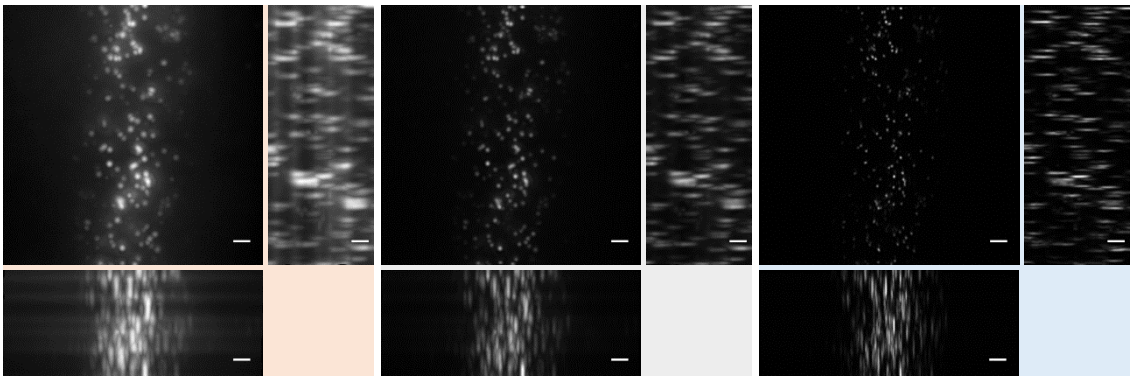

Fig. S12. Maximum intensity projection of conventional wide-field (summedWF), deconvolved wide-field (decWF) and structured illumination (SIall) image stacks. We first corrected the drift of the planes in the z-stack by the StackReg plugin of ImageJ with the translation transformation. We performed the maximum intensity projections in xy-, xz-, and yz-planes. The lateral resolution is dramatically improved in SIall, while the axial resolution (880.29±72.84 nm) remains similar to that in summedWF and decWF since our light sheet is still thicker than the axial PSF of detection lens. The sample consists of 40 nm beads embedded in 1.5% low-melt agarose. The periods of three interference pattern orientations used in this acquisition are 300.9 nm, 263.8 nm, and 262.9 nm. The pattern orientations are 0°, 50°, and 133°. The stack is acquired with an axial spacing of 200 nm and 30 axial planes. All scale bars are 1 μm wide.

Note 14: Quantification of the resolution improvement of the high-resolution image stack

A. Selected images for resolution measurement

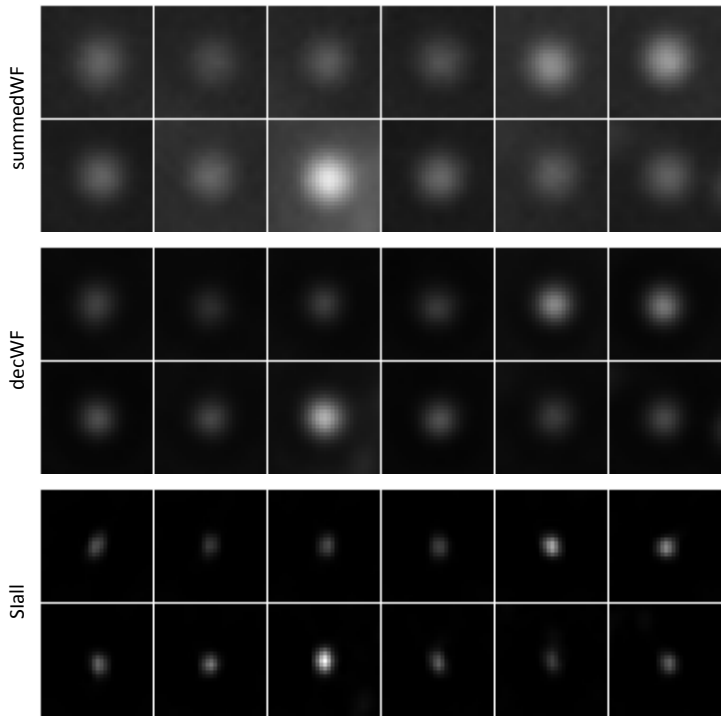

B. Resolution measurement

	summedWF		decWF		SIall	
	x	y	x	y	x	y
Bead1	287.0	310.6	227.6	251.9	107.5	138.0
Bead2	280.7	292.3	223.8	231.0	102.2	135.7
Bead3	262.2	269.3	211	222.0	105.4	132.7
Bead4	287.7	281.8	230.8	222.1	107.8	136.7
Bead5	275.2	275.6	211.6	213.0	101.7	118.5
Bead6	273.1	282.8	210.4	218.2	114.3	118.4
Bead7	276.6	284.8	209.7	210.2	106.5	130.8
Bead8	267.8	288.9	215.2	228.0	100.1	116.1
Bead9	295.1	285.8	221.0	220.7	99.7	131.1
Bead10	279.8	289.9	214.0	223.2	94.7	135.5
Bead11	279.8	293.8	218.2	229.5	105.1	145.2
Bead12	297.4	269.6	228.4	219.8	110.4	123.7
ave	**280.2**	**285.4**	**218.5**	**224.1**	**104.6**	**130.2**
stdev	**10.39**	**11.33**	**7.65**	**10.68**	**5.29**	**9.10**
ration_y/x		**1.02**		1.03		1.24
correction	**280.2**	**280.2**	**218.5**	**220.0**	**104.6**	**127.8**

Fig. S13. Measuring the resolution in an image stack. The image stacks in this example are the stacks shown in fig. S12. Since it is a three-dimensional image we looked for the focus of each bead image and cropped the bead image in its focal plane. E.g. the selected images shown in (A) are distributed along different planes in the whole image stack. Next, we fitted each cropped image with a two-dimensional Gaussian curve with *Mathematica* as described previously. The cropped images of identical beads in the summedWF, decWF and SIall images are shown in (A). (**B**) The result of the resolution measurement. We also noticed the same effect that the average resolutions in x and y are not similar as previously shown in fig. S10. Therefore, we used the same method as described previously to correct the values of final

resolutions. Finally, we obtained the resolutions of the conventional wide-field image, deconvolved wide-field image, and SIall image are 280.2±10.39 nm (x) and 280.2±11.12 nm (y), 218.5±7.65 nm (x) and 220.0±10.49 nm (y), and 104.6±5.29 nm (x) and 127.8±8.93 nm (y), respectively. The obtained resolutions are essentially similar to the values obtained previously (Fig. S10). In summary, the resolution improvement in the x-axis of SIM image compared to conventional wide-field image and the deconvolved wide-field image is 2.7x and about 2.1x, respectively. Even along the y-axis, the resolution improvement reaches 2.2x and 1.7x as compared to conventional wide-field image and deconvolved wide-field image, respectively. The ratio of the resolution between y- and x-axis in SIM image is 1.22x (127.8/104.6), which is also similar to the value obtained previously (Fig. S11).

Note 15. High-resolution image stack with counter-propagating light sheets

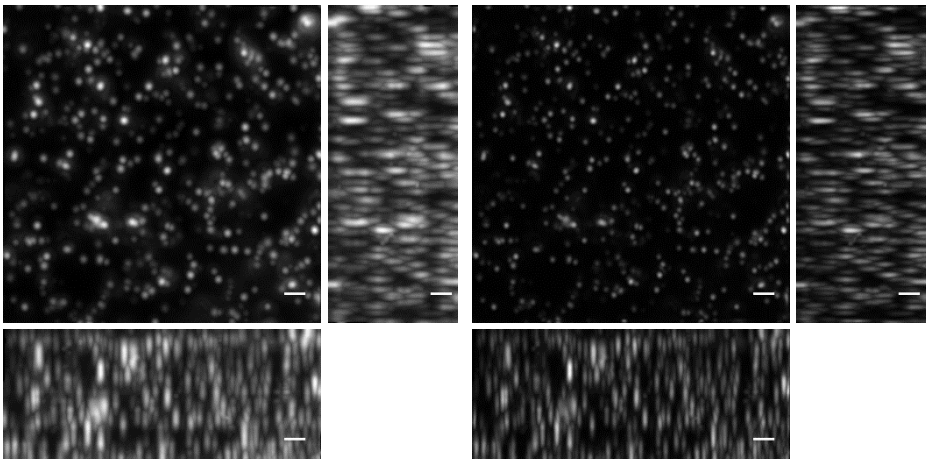

summedWF decWF

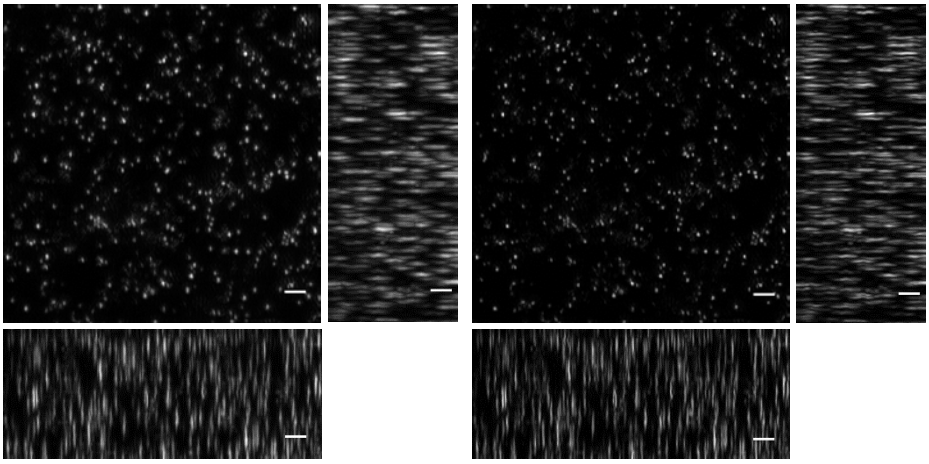

SIall without continued deconvolution SIall

Fig. S14. Maximum intensity projection of image stacks of conventional wide-field (summedWF), deconvolved wide-field (decWF), structured illumination without continued deconvolution and structured illumination (SIall), with counter-propagating light sheets. We first corrected the drift of the planes in the z-stack by the StackReg plugin in ImageJ with translation transformation. Next, we scaled the image stack 2x laterally and 6.94x axially by ImageJ with bicubic interpolation. This results in a voxel size of 28.8x28.8x28.8 nm^3. Finally, we performed the maximum intensity projections in xy-, xz-, and yz-planes. The lateral resolution is dramatically improved in SIall with and without the continued deconvolution, while the axial resolution (880.29±72.84 nm) remains similar to that in summedWF and decWF since our light sheet is still thicker than the axial PSF of detection lens. The noisy patches are removed and the resolution is improved with the continued deconvolution (SIall). The sample consists of 40 nm beads embedded in 1.5% low-melt agarose. The three pattern orientations used here are 0°, 31°, and 146°. The stack is acquired with an axial spacing of 200 nm and 30 axial planes. All scale bars are 1 μm wide.

Note 16: The power spectra of super-resolution images with counter-propagating light sheet illumination

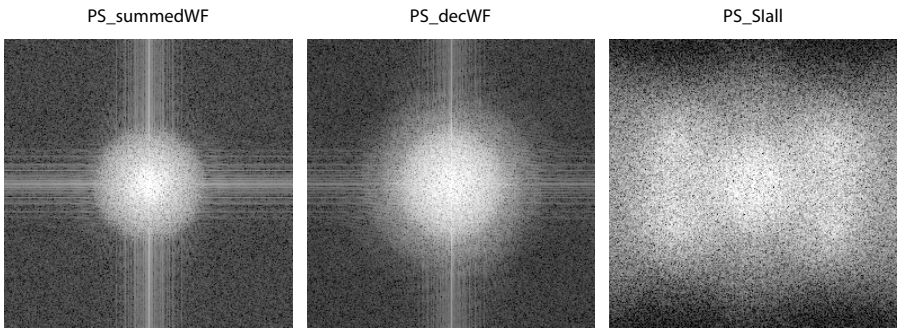

Fig. S15. Power spectra of the images shown in fig. 4. The power spectra were calculated with ImageJ's FFT function, which uses a logarithmic scaling.

Note 17: Quantification of the resolution improvement of the high-resolution image stack

	summedWF		decWF		SIM w/o cont'd-dec.		SIall	
	x	y	x	y	x	y	x	y
Bead1	283.0	292.1	214.9	218.8	113.6	167.3	98.5	119.6
Bead2	281.5	281.0	209.2	212.5	96.0	164.3	68.1	120.5
Bead3	276.0	275.7	207.6	213.0	102.6	153.8	70.6	116.1
Bead4	278.4	278.0	209.5	206.9	115.7	148.1	98.1	107.8
Bead5	281.7	281.0	214.7	220.1	116.7	161.3	99.7	123.8
Bead6	287.1	301.0	214.6	232.8	117.4	194.2	79.1	153.0
Bead7	282.9	276.5	209.2	212.0	117.1	145.6	94.5	109.3
Bead8	279.8	281.0	211.7	220.5	134.6	165.0	96.9	114.5
Bead9	278.4	302.0	214.4	254.3	132.1	210.5	86.9	160.3
Bead10	288.2	282.7	214.8	213.4	125.8	188.6	105.8	135.9
Bead11	280.5	273.7	216.1	237.7	110.8	173.4	105	132.7
Bead12	278.6	273.7	211.5	219.0	109.5	153.6	96.7	117.9
Bead13	278.8	292.0	202.4	221.4	123.3	213.4	100.2	165.4
Bead14	270.8	275.6	202.3	210.0	105.8	174.0	81.7	125.1
Bead15	288.0	279.5	214.8	209.7	121.0	166.2	91.1	117.5
Bead16	277.6	284.0	205.6	216.2	116.4	180.5	99.3	136.4
Bead17	309.4	307.0	230.7	239.2	112.1	156.4	81.7	122.3
Bead18	268.7	279.1	200.2	214.0	95.3	160.6	60.0	121.4
Bead19	320.0	289.4	241.5	227.8	104.6	165.2	71.8	131.9
Bead20	270.6	254.7	190.9	200.0	110.6	159.8	99.7	114.8
ave	**283.0**	**283.0**	**211.8**	**220.0**	**114.1**	**170.1**	**89.3**	**127.3**
stdev	**12.18**	**11.81**	**10.60**	**12.82**	**10.43**	**18.85**	**13.47**	**16.11**

Table S1. Resolution measurement of conventional wide-field (summedWF), deconvolved wide-field (decWF), structured illumination without continued deconvolution (SIM w/o cont'd-dec.) and structured illumination (SIall), with counter-propagating light sheets. The resolutions are measured from the dataset shown in fig. S14. The measuring process is the same as previously described in fig. S11. We obtained the resolutions of the conventional wide-field image, deconvolved wide-field image, SIall without continued deconvolution and SIall image are 283.0±12.18 nm (x) and 283.0±11.81 nm (y), 211.8±10.60 nm (x) and 220.0±12.82 nm (y), 114.1±10.43 nm (x) and 170.1±18.85 nm (y), and 89.3±13.47 nm (x) and 127.3±16.11 nm (y), respectively.

Note 18: Pattern periods and achieved resolution at different intersection angle

A

	Pattern1			Pattern2			Pattern3		
	period (nm)	intersection angle (°)	rotation angle (°)	period (nm)	intersection angle (°)	rotation angle (°)	period (nm)	intersection angle (°)	rotation angle (°)
a	307.2	73.4	0.0	274.4	84.0	45.0	274.4	84.0	135.0
b	239.8	99.8	0.0	223.0	110.8	46.5	220.7	112.4	135.3
c	183.1	180.0	0.0	183.9	172.0	29.9	184.7	166.8	152.8

B

	summedWF			decWF			SIall		
	x (nm)	y (nm)	y/x	x (nm)	y (nm)	y/x	x (nm)	y (nm)	y/x
a	285.4±11.85	285.4±17.32	1.00	225.7±11.70	227.5±17.21	1.01	103.0±6.35	129.1±10.32	1.25
b	285.0±15.86	285.0±15.62	1.00	232.8±9.56	233.8±10.63	1.01	97.8±11.47	117.4±10.92	1.20
c	283.0±12.18	283.0±11.81	1.00	211.8±10.60	220.0±12.82	1.04	89.3±13.47	127.3±16.11	1.43

Table S2. Quantified summary of the images shown in Fig. 5. In both (A) and (B), a, b and c denote the case (A), (B) and (C), respectively in fig. 5. (**A**) Parameters of the interference pattern. Period, intersection angle and rotation angle denote the period of the interference pattern, the intersection angle of two light sheets and the rotation angle of the pattern, respectively. Pattern1, Pattern2 and Pattern3 denote the three rotation orientations of the pattern. As shown, the periods of the patterns in fig. 5A are close to the diffraction limit, whereas the periods of the patterns in fig. 5B and fig. 5C are beyond the diffraction limit of the objective lens. Both rotation angles of the patterns in fig. 5A and fig. 5B can reach up to 45°, whereas they are around 27° in fig. 5C. (**B**) Resolutions and their ratios of y- to x-axis of summedWF, decWF and SIall images. The numbers in each case were given by an average of more than 20 measurements. All values are corrected when a falling of the gel, as previously described, is noticed. The resolutions of summedWF are in all cases similar at around 280 nm to 290 nm. The resolutions of decWF are better in the counter-propagating case and we consider this is due to a lower background in the image. The resolution along the x-axis improves with a finer period of the pattern. The y/x ratios of SIall of cases a and b are similar since the rotation angles of Pattern2 and Pattern3 are similar. The y/x-ratios of SIall in case c are larger than those in case a and case b because the rotation angle is smaller. Finally, we conclude that case b is indeed a good compromise since the x-resolution is better than 100 nm and the y-resolution is about 100 nm, while the y/x-ratio of the resolution is optimal with the current choice of the illumination objective lens.

Note 19: Illumination area along z of oblique light sheet illumination

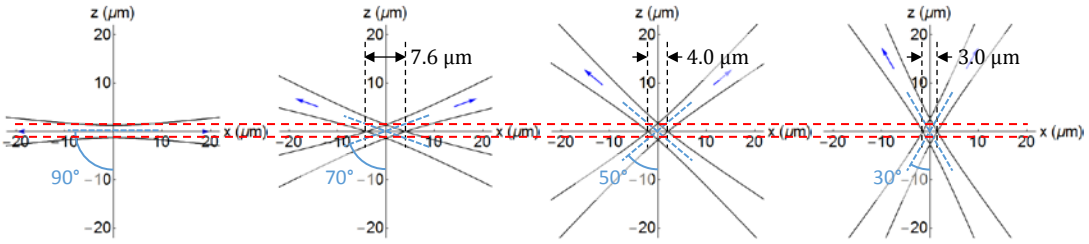

Fig. S16. Illumination area along z for different oblique configurations of light sheets. The axial resolution of our current setup is not affected by the oblique illumination-detection configuration since the current thickness of our light sheets is about 2.6 μm, which is larger than the axial PSF of detection lens. Nevertheless, the image contrast is dramatically improved by the light sheet illumination. The red lines indicate the thickness of the light sheets. The intersection areas of two light sheets are marked, however, the practical FOV will be slightly larger than these areas, such as those indicated in Fig. 5. The optimal image contrast is obtained with an orthogonal illumination-detection configuration, in which the light sheet illuminates the thinnest region along z (the leftmost sketch). The illumination extent along z is increased since the light sheets are more oblique, but only significant in the rightmost sketch. I.e., the image contrast is only reduced at this oblique configuration. The contribution of the background with different illumination conditions is discussed in the manuscript (section “Near-isotropic high-resolution image at sub-100 nm” and Fig. 5). The sketches are calculated with *Mathematica* and the light sheet profile is plotted according to the Gaussian beam propagating equation.

Note 20: Other high-resolution images of live yeast cells

A. Maximum intensity projection of decWF

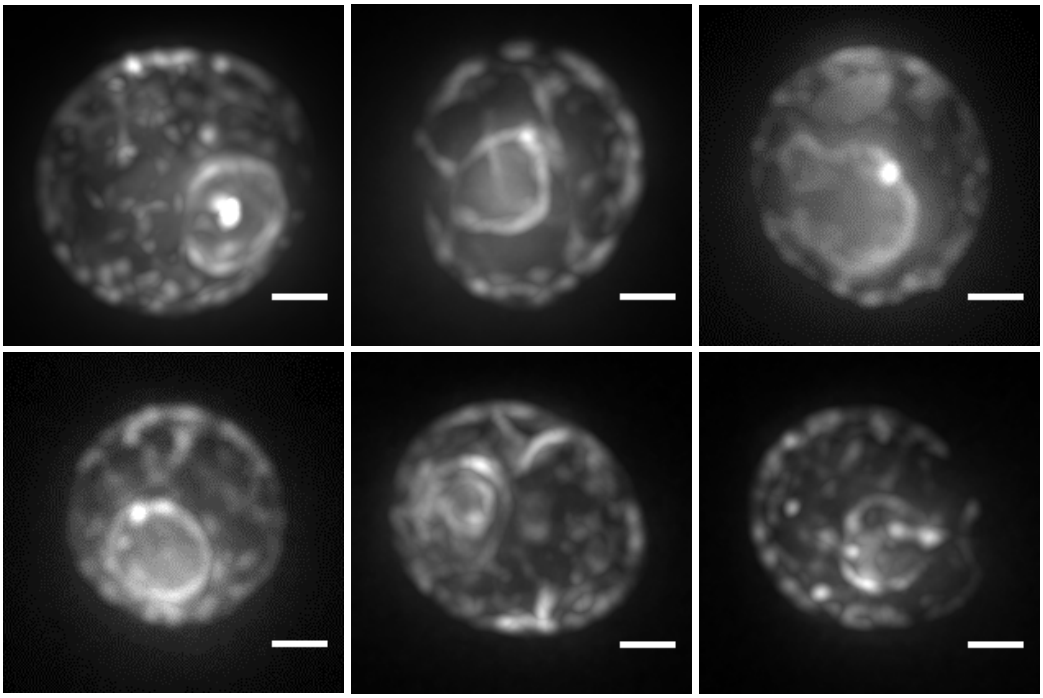

B. Maximum intensity projection of SIall

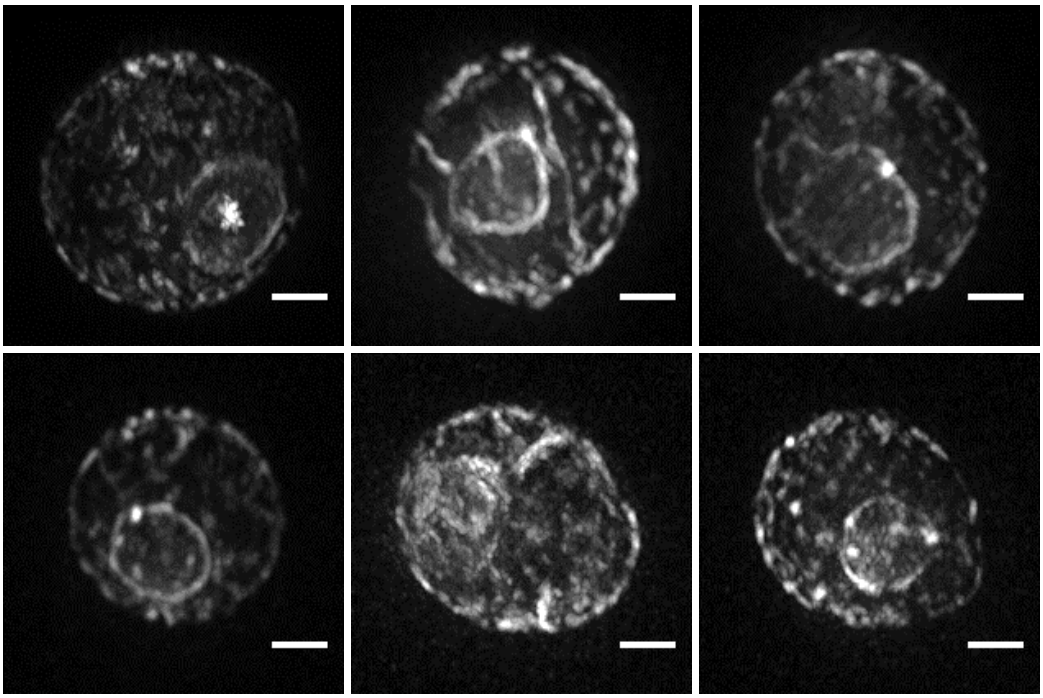

Fig. S17. Six further images of live yeast embedded in 1.5% low-melt agarose. The structure shown here is also GFP-tagged endoplasmic reticulum (ER). (**A**) Maximum intensity projections of deconvolved wide-field image stacks. (**B**) Maximum intensity projections of SIM image stacks. All scale bars are 1 µm wide.

Note 21: Other high-resolution images of live yeast cells

A. Maximum intensity projection of central ten planes of decWF

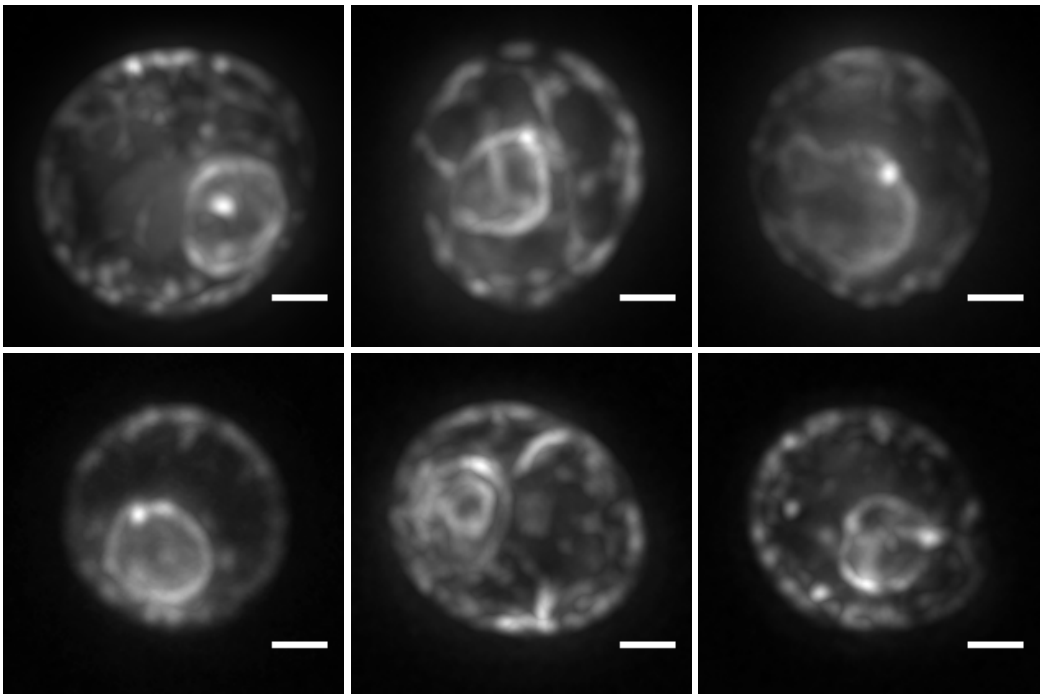

B. Maximum intensity projection of central ten planes of SIall

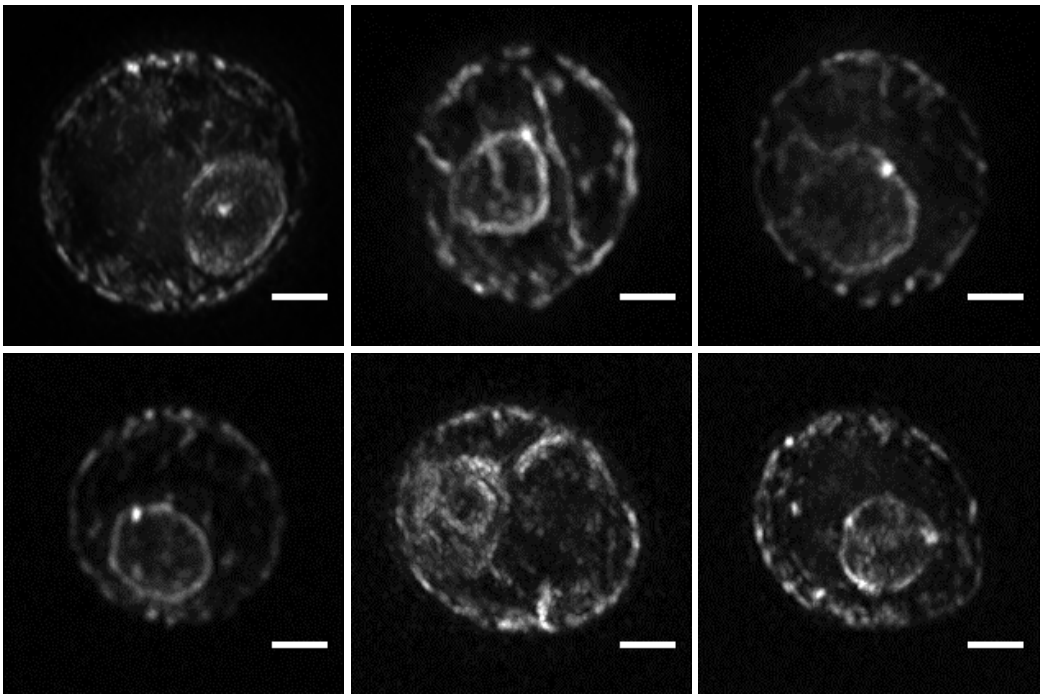

Fig. S18. Maximum intensity projections of the central ten planes of the same image stacks shown in fig. S17. (**A**) Deconvolved wide-field images. (**B**) SIM images. This method of projection excludes more out of focus images and allows us to see the main structure in the middle of the six cells more clearly. All scale bars are 1 µm wide.

Note 22: High-resolution images of fixed yeast cells

A. Maximum intensity projection of whole stack

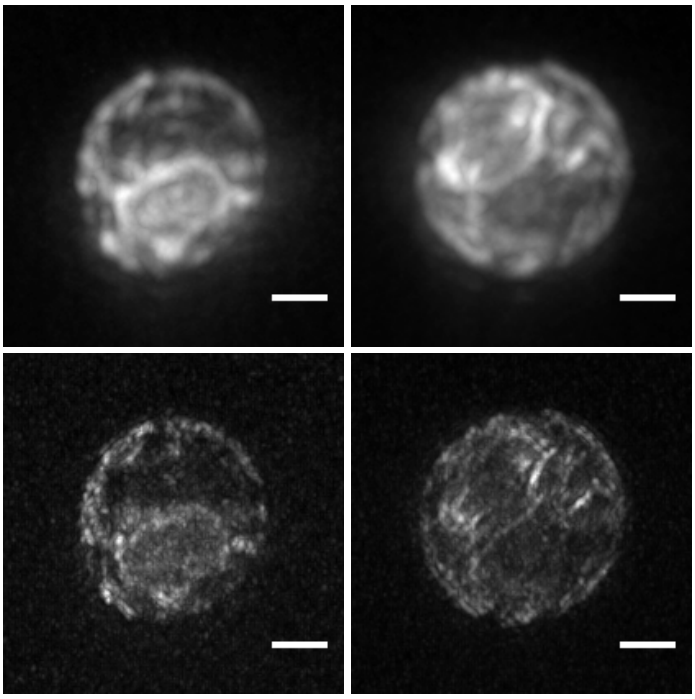

B. Maximum intensity projection of central ten planes

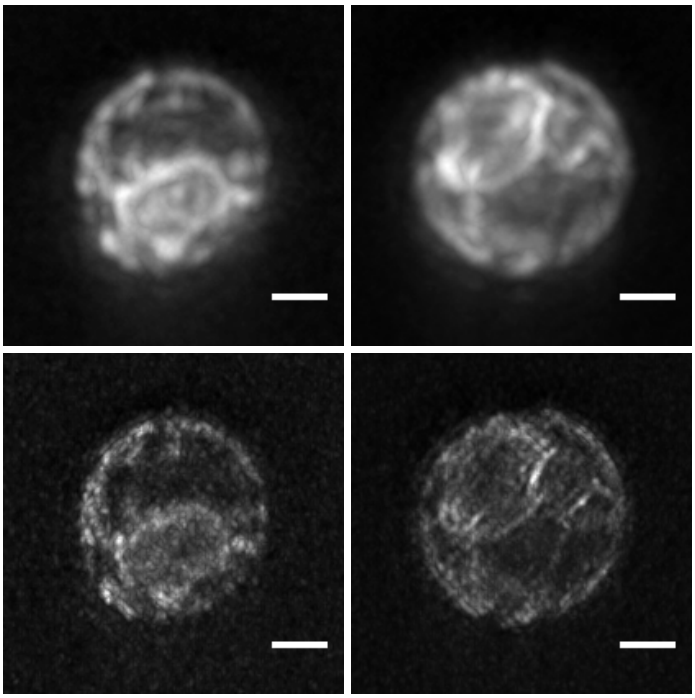

Fig. S19. Images of GFP-tagged Endoplasmic reticulum (ER) of fixed yeast cell. The cells are fixed with 4% paraformaldehyde at 37°C for 8 min and then embedded in 1.5% low-melt agarose. (**A**) Comparison of the maximum intensity projections between deconvolved wide-field and SIM image stack. (**B**) Comparison of the maximum intensity projections in the middle ten planes between deconvolved wide-field and SIM image stack. Unlike the images shown in fig. S17 and fig. S18, the images in (A) and (B) are

quite similar. The structures of ER shown here do not look similar to those in the live yeast, indicating our fixation process damages the cell. The difference of the ER structure between fixed and live cells does not appear so clearly in the wide-field or deconvolved wide-field images but is very obvious in the SIM images. The image stacks shown here consist of 50 axial planes with an axial spacing of 200 nm. All scale bars are 1 µm wide.

Note 23: Biological images with SIM pattern at large intersection angles

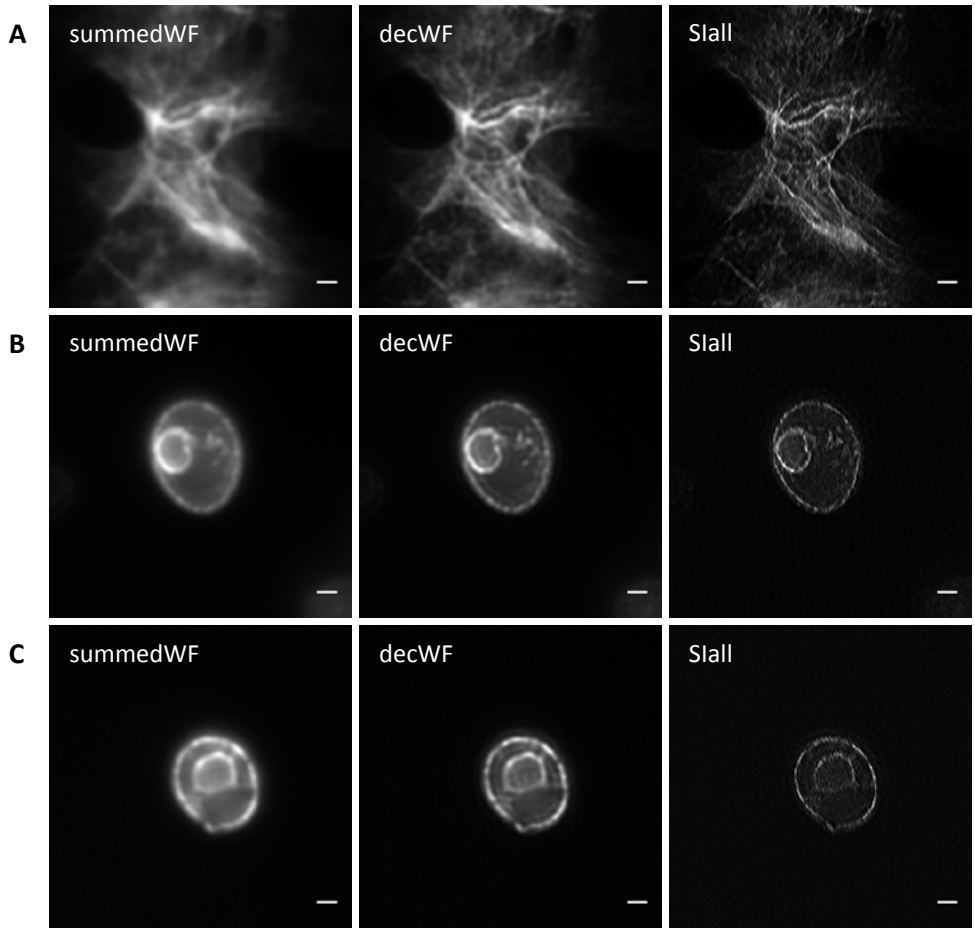

Fig. S20. Preliminary result of biological images with SIM patterns at large intersection angles. A current challenge of csiLSFM is to properly mount the sample, which however is not directly related to the set-up. A possible solution is to mount the sample on a transparent film with the refractive index close to water, such as FEP (Fluorinated ethylene propylene) or Lumox (https://www.sarstedt.com) film. When using an FEP film, we first treated it with oxygen plasma and then coated it with 5mM APTS ((3-aminopropyl)triethoxysilane). (**A**) Actin filaments of the HC11 cell. The cells were cultured on FEP film, and then fixed with 4% paraformaldehyde and the actin was labeled with Alexa488. (**B, C**) GFP-tagged ER of yeast. The cell was seeded on Lumox film and covered with 1% low melt agarose. (**A, B**) The intersection angle of two light sheets is 130°, which creates a period of about 202 nm of the SI pattern. (**C**) Light sheets are counter-propagating that creates the finest period of 183 nm. All scale bars are 1 μm wide. A little zig-zag pattern seems to be appeared in (**C**). This is probably due to the rapid movement of the ER structure in the living cell(21). Please note that the images shown here were taken with large intersection angles thus the resolution gain is more anisotropic and very high (>2x). Therefore, the sample features along the x-axis are perceived as discrete whereas they look more continuous along the y-axis. This could increase the influence of the rapid movement of the sample to the SIM reconstruction that results in a more obvious zig-zag pattern.

Note 24: Retrieving pattern frequency

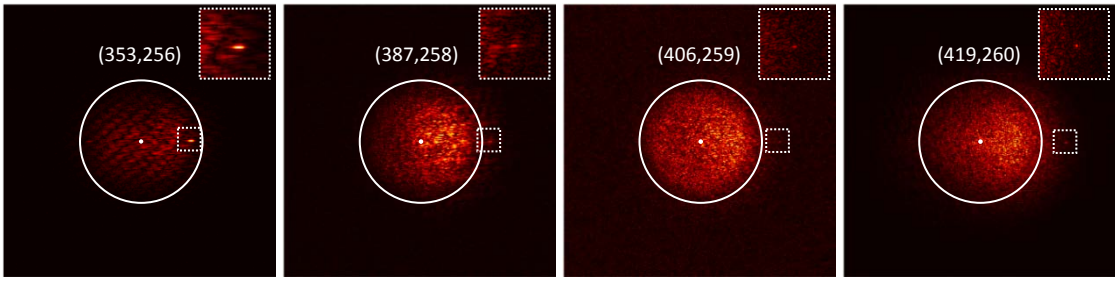

$\theta = 36.7°$ $\theta = 54.0°$ $\theta = 68.0°$ $\theta = 90°$

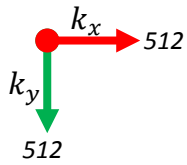

$\vec{p}_j = \frac{2\pi}{(Pixelsize)(Image\ length)}\left((k_x, k_y) - (k_{xo}, k_{yo})\right)$, eq. 1

(k_x,k_y) = Peak position in the correlation

(k_{xo},k_{yo}) = Image center position

Pixelsize = Center-center distance of two pixels in length units

Image length = Defined for a squared pixel array as the maximum number of pixels along one dimension.

$p_j = \|\vec{p}_j\|$, eq. 2

$T_0 = \frac{2\pi}{p_j}$, eq. 3, where T_0= Period of the illumination pattern

$T_0 = \frac{\lambda_{exc}}{2nsin(\theta)}$, eq. 4, where θ = Beams interference half-angle

Fig. S21. Correlations between the central and extended bands for the first pattern orientation, ca. 0°, for different pattern periods. The correlation yields a sharp peak, whose position determines the spatial frequency of the pattern. Notice how the position of the peak shifts away from the center (white dot at (k_{xo},k_{yo})=(257,257)) as the interference angle of the beams increases. This is expected since the spatial frequency of the pattern increases with an increasing angle θ according to equations 3 and 4. The position of the peak (k_x,k_y) shown in the parentheses is substituted in eq. 1 to convert the pixel position into the spatial frequency vector $\vec{p}$. A prior deconvolution of the raw images enhances the detectability of the peak in the correlation. This allows us to recover $\vec{p}$, even when it lies beyond the cut-off frequency ω_o (radius of the white circle) of the detection objective. The recovered $\vec{p}$ is also used to characterize our system and, as shown in fig. S22, confirms that all measurements are reasonable and that the system is well aligned. All figures are derived from actual data obtained with 200 nm fluorescent beads (505nm/515nm; excitation/emission).

Note 25: System characterization with a calibration curve

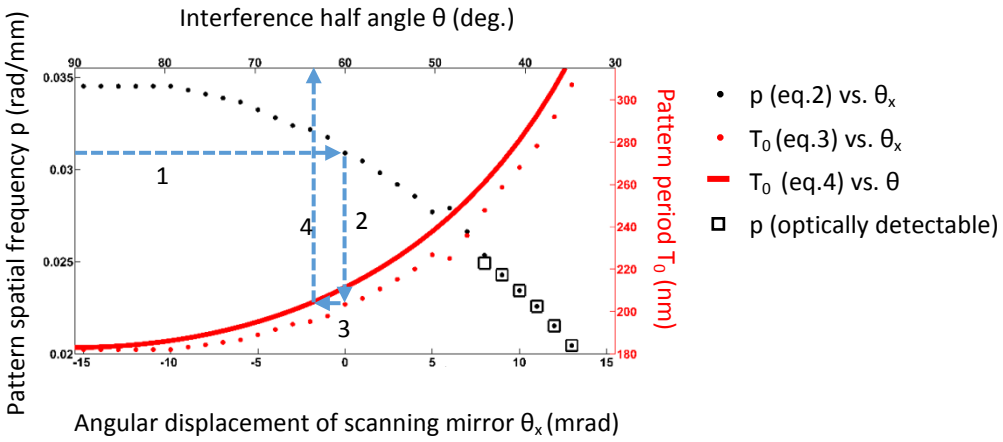

Fig. S22. Calibration curve of the interference half angle θ of two light sheets (beams) as a function of the angular displacement of the two-axes scanning mirror. Blue dashed arrows 1 to 4 essentially show the workflow of the calibration curve. First, we obtain the norm of $\vec{p}_j$ (black dots) and pattern period T_0 (red dots) (eq. 2 and eq. 3 in fig. S20) at different angular displacements θ_x of the scanning mirror. Next, the red curve represents the theoretical calculation of the pattern period T_0 against the interference half angle θ (eq. 4). By comparing the red dots and the red curve, we extract the approximated value of the interference half angle θ. The result corresponds to the 200 nm beads dataset used for fig. S18. Three important features in the curve are: (1) $\theta_x = 0$ is the position, at which the beams hit the center of the back aperture of their corresponding illumination objectives and travel parallel to the illumination objective long axis. The intersection angle of the two illumination objectives is ideally 130° as shown in fig. 3C. According to the calibration curve the interference half angle at this position ($\theta_x = 0$) is 63°, which doubled provides the approximation126°. (2) The minimum theoretical value of T_0 is 183 nm at θ = 90° for n = 1.33 and λ_{exc} = 488 nm. This corresponds very well with the experimental value of 182 nm, which is the largest spatial frequency 0.0345 rad /nm achieved in csiLSFM. (3) Seven points marked by the center of the black squares are added to show the frequencies that can be detected optically. These were obtained by directly measuring the frequency from the Fourier transform of the pattern at different θ_x. The center of the squares matches the frequency obtained from the correlation peaks in the beads dataset. The last frequency recorded before the pattern is no longer visible in the image plane is 0.0251 rad/nm. This value characterizes the cut-off frequency of our detection objective. From the calibration curve, this spatial frequency is associated to a period of 250 nm and an interference half angle of 45°. Both values correspond with the theoretical value of the resolution at a wavelength of 488 nm (244 nm, Abbe's formula) and the angular aperture of our detection objective 48° = $\sin^{-1}(1/1.33)$.

Note 26: Effects of iteration in Richardson-Lucy deconvolution

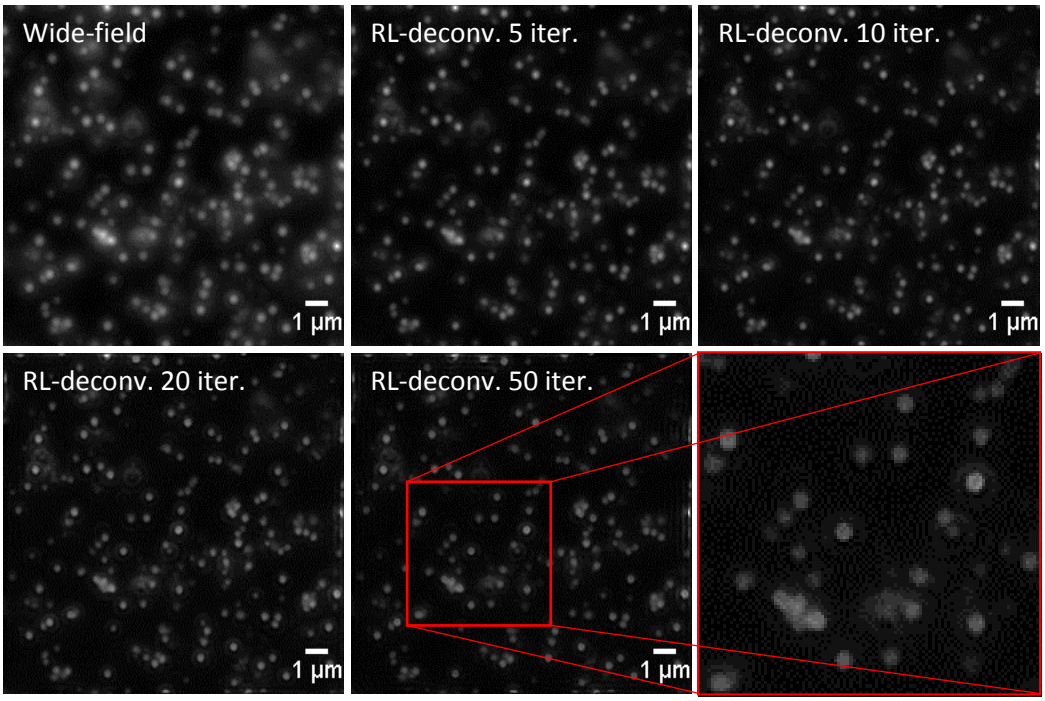

Fig. S23. Maximum intensity projection of image stacks of 40 nm beads with different iterations in the Richardson-Lucy (RL) deconvolution. RL deconvolution removes the out of focus fluorescence. The images after five and ten iterations look similar. But, artifact starts to appear after 20 iterations are applied in the RL deconvolution. The artifact becomes even more obvious after 50 iterations: the images of beads appear to be hollow at their center. The dataset used here is the same as the one in fig. S14, where the sample is illuminated with counter-propagating light sheets. The original image stack consists of 30 planes, but the images presented here were calculated with the maximum intensity projection of the central ten planes, to show the artifact more clearly. The RL-deconvolution is applied directly on the summed wide-field images plane-wise.

References

1. Greger K, Swoger J, Stelzer EHK (2007) Basic building units and properties of a fluorescence single plane illumination microscope. *Rev Sci Instrum* 78(2):23705.
2. Stelzer EHK (1998) Contrast, resolution, pixelation, dynamic range and signal-to-noise ratio: fundamental limits to resolution in fluorescence light microscopy. *J Microsc* 189(1):15–24.
3. Perez V, et al. (2016) Optimal 2D-SIM reconstruction by two filtering steps with Richardson-Lucy deconvolution. *Sci Rep* 6:37149.
4. Chang B-J, Chou L-J, Chang Y-C, Chiang S-Y (2009) Isotropic image in structured illumination microscopy patterned with a spatial light modulator. *Opt Express* 17(17):14710–14721.
5. Gustafsson MGL, Agard DA, Sedat JW (2000) Doubling the lateral resolution of wide-field fluorescence microscopy using structured illumination. *BiOS 2000 The International Symposium on Biomedical Optics*, eds Conchello J-A, Cogswell CJ, Tescher AG, Wilson T (International Society for Optics and Photonics), pp 141–150.
6. Gustafsson MGL, et al. (2008) Three-dimensional resolution doubling in wide-field fluorescence microscopy by structured illumination. *Biophys J* 94(12):4957–70.
7. Rasband WS ImageJ. Available at: http://imagej.nih.gov/ij/.
8. Min J, et al. (2013) Fluorescent microscopy beyond diffraction limits using speckle illumination and joint support recovery. *Sci Rep* 3:2075.
9. Keller PJ, et al. (2010) Fast, high-contrast imaging of animal development with scanned light sheet-based structured-illumination microscopy. *Nat Methods* 7(8):637–42.
10. Reynaud EG, Krzic U, Greger K, Stelzer EHK (2008) Light sheet-based fluorescence microscopy: more dimensions, more photons, and less photodamage. *HFSP J* 2(5):266–75.
11. Chen B-C, et al. (2014) Lattice light-sheet microscopy: Imaging molecules to embryos at high spatiotemporal resolution. *Science* 346(6208):1257998–1257998.
12. Ingaramo M, et al. (2014) Richardson-Lucy Deconvolution as a General Tool for Combining Images with Complementary Strengths. *ChemPhysChem* 15(4):794–800.
13. Richardson WH (1972) Bayesian-Based Iterative Method of Image Restoration. *J Opt Soc Am* 62(1):55.
14. Lucy LB (1974) An iterative technique for the rectification of observed distributions. *Astron J* 79:745.
15. Planchon TA, et al. (2011) Rapid three-dimensional isotropic imaging of living cells using Bessel beam plane illumination. *Nat Methods* 8(5):417–23.
16. Ströhl F, Kaminski CF (2015) A joint Richardson—Lucy deconvolution algorithm for the reconstruction of multifocal structured illumination microscopy data. *Methods Appl Fluoresc* 3(1):14002.
17. Komis G, et al. (2015) Superresolution live imaging of plant cells using structured illumination microscopy. *Nat Protoc* 10(8):1248–1263.
18. Wolfram Research I (2014) Mathematica. Available at: http://www.wolfram.com/mathematica/.
19. Fedosseev R, Belyaev Y, Frohn J, Stemmer A (2005) Structured light illumination for extended resolution in fluorescence microscopy. *Opt Lasers Eng* 43(3–5):403–414.

20. Heintzmann R, Cremer CG (1999) Laterally modulated excitation microscopy: improvement of resolution by using a diffraction grating. *BiOS Europe '98*, eds Bigio IJ, Schneckenburger H, Slavik J, Svanberg K, Viallet PM (International Society for Optics and Photonics), pp 185–196.

21. Kner P, Chhun BB, Griffis ER, Winoto L, Gustafsson MGL (2009) Super-resolution video microscopy of live cells by structured illumination. *Nat Methods* 6(5):339–42.